EDGE ARTICLE

Check for updates

Electronic metal–support interaction induces electron deficiency in iridium for promoted ampere-grade-current-density electrocatalytic hydrogen evolution

Linfeng Zhang,[a] Weimo Li,[a] Siyu Ren,[a] Yue Zhang,[a] Wei Song, [b] Ce Wang [a] and Xiaofeng Lu [*a]

Precise manipulation of the metal–support interaction offers a powerful approach for tailoring the electronic properties of electrocatalysts and driving superior hydrogen evolution reaction (HER) performance. However, achieving high catalytic performance at ampere-level current densities remains a formidable challenge. Herein, an iridium–cobalt phosphide heterostructure anchored on carbon nanofibers (Ir–CoP/CNFs) is constructed to boost the electrocatalytic HER performance. In this catalyst, the electronic metal–support interaction (EMSI) induces an electron deficiency in Ir, which modulates its electronic structure and effectively mitigates excessive H* intermediate adsorption. This electronic modulation greatly reduces the energy barrier for water dissociation, endowing the catalyst with exceptional alkaline/acidic-universal HER activity. Remarkably, the Ir–CoP/CNFs catalyst presents higher HER activity than Pt/C at ampere-grade current density, achieving overpotentials of merely 117 mV in 0.5 M H_2SO_4 and 235 mV in 1.0 M KOH at 1000 mA cm^{-2}. These values rank among the best-reported performance for HER electrocatalysts. Moreover, this catalyst also demonstrates superior durability compared to Pt/C. This study underscores the impact of EMSI on enhancing HER performance at high current densities, paving the way for the development of high-efficiency next-generation HER electrocatalysts.

1. Introduction

The pervasive reliance on fossil fuels has precipitated profound environmental consequences, fueling global warming and intensifying air pollution. To address these pressing challenges, there is a burgeoning global focus on the advancement of clean energy technologies.[1,2] Among renewable energy options, hydrogen (H_2) stands out due to its high energy density and zero carbon combustion, with diverse applications.[3–5] Unlike solar and wind power, it boasts advantages such as long-term storability and infrastructure compatibility, crucial for future energy systems.[6–9] Electrocatalytic water splitting is pivotal for clean H_2 production, entailing the hydrogen evolution reaction (HER) at the cathode and the oxygen evolution reaction (OER) at the anode, powered by renewable energy.[10,11] The efficiency of this process is largely governed by the HER and OER electrocatalysts, which minimize overpotentials and accelerate reaction kinetics.[12–14] Iridium (Ir)-based materials are esteemed as

state-of-the-art catalysts for the HER, renowned for their remarkable catalytic activity, robust stability under severe conditions, and excellent corrosion resistance.[15–17] Nevertheless, their practical deployment faces significant hurdles. For instance, Ir-based catalysts typically require high overpotentials to achieve industrially relevant current densities (>1 A cm^{-2}), resulting in substantial energy losses that compromise the overall efficiency of water splitting.[18,19] Moreover, the high cost of Ir and its ultra-low natural abundance present substantial economic and resource barriers to widespread adoption.[20] Thus, developing high-efficiency HER catalysts with low Ir content at industrial-level current densities constitutes a critical research direction.

To surmount the challenges outlined, various strategies have been explored for creating high-performance HER catalysts, such as engineering multi-metal heterostructures, modifying surface ligands, and tuning the electronic metal–support interaction (EMSI).[21–26] EMSI refers to the modulation of charge distribution between metallic nanoparticles and their support, significantly boosting hydrogen adsorption/desorption kinetics. Transition metal phosphides (TMPs) are renowned for their exceptional HER activity and relatively low cost.[27–29] Among TMPs, cobalt phosphide (CoP) distinguishes itself through its

[a]Alan G. MacDiarmid Institute, College of Chemistry, Jilin University, Changchun 130012, P. R. China. E-mail: xflu@jlu.edu.cn

[b]State Key Laboratory of Supramolecular Structure and Materials, College of Chemistry, Jilin University, Changchun 130012, P. R. China

superior electrical conductivity, structural tunability, and chemical stability. Additionally, CoP exhibits moderate hydrogen adsorption/desorption characteristics, making it an ideal support material for designing high-performance HER catalysts.[30–32] Notably, a Ru/CoP heterostructure constructed *via* an impregnation–phosphorization process demonstrates outstanding alkaline HER performance, achieving low overpotentials comparable to those of Pt/C at low current densities.[33] This superior activity arises from the metal–support interactions that facilitate charge transfer and optimizes the hydrogen adsorption energy. Nevertheless, enhancing the HER performance of the catalyst across a wide pH range and at high current densities remains crucial for realizing its potential for industrial applications.

In this study, we reported a reliable synthetic approach to construct Ir/CoP heterostructures supported on carbon nanofibers (Ir–CoP/CNFs) for acidic/alkaline-universal HER application. Spectroscopic and electrochemical analyses exhibit efficient electron transfer from Ir to CoP through EMSI, which optimizes the adsorption of the H* intermediates on the catalyst and effectively lowers the energy barrier of the rate-determining step in the HER pathway. Furthermore, the CNF

substrate exhibits superior electrical conductivity and facilitates the dispersion of active sites. Therefore, it exhibits better acidic and alkaline HER activities than the commercial Pt/C benchmark at ampere-level current densities. Specifically, the optimized Ir–CoP/CNFs catalyst achieves a mass activity (MA, A g_{NM}^{-1}) up to 7.8-fold in acidic electrolyte and 3.8-fold in alkaline solution of the commercial Pt/C catalyst. Compared to Pt/C, the catalyst shows superior long-term stability. These findings highlight the promising route with EMSI to design high-performance HER catalysts, paving the way for scalable H_2 hydrogen production technologies.

2. Results and discussion

2.1 Synthesis and characterization of Ir–CoP/CNFs

The synthesis protocol for the 600Ir–CoP/CNFs is illustrated in Fig. 1a. Morphological evolution of the samples throughout the synthesis process is systematically examined using field-emission scanning electron microscopy (FE-SEM) and transmission electron microscopy (TEM). The precursor nanofibers, incorporating cobalt acetate, are successfully fabricated *via* an electrospinning technique, exhibiting an average diameter of
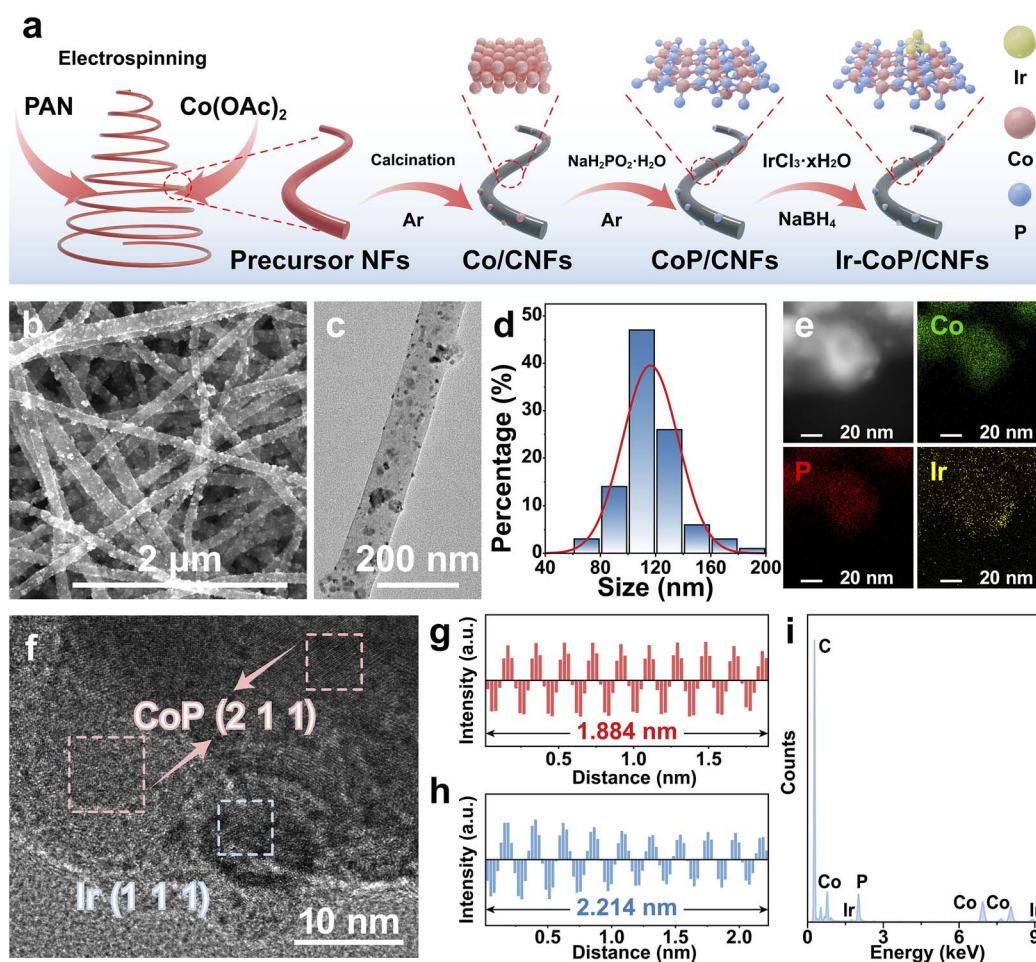

Fig. 1 (a) Synthetic route illustration for Ir–CoP/CNFs. (b) SEM, (c) TEM, and (d) diameter distribution of 600Ir–CoP/CNFs. (e) Elemental mapping of Co, P, and Ir elements of 600Ir–CoP/CNFs. (f) HRTEM image of 600Ir–CoP/CNFs. FFT-based crystal plane spacing distribution histogram of (g) CoP (211) and (h) Ir (111). (i) EDX spectrum of 600Ir–CoP/CNFs.

approximately 246 nm (Fig. S1, SI). Subsequent calcination of these precursor nanofibers under an argon (Ar) atmosphere yields Co/CNFs with a significantly reduced fiber diameter, attributable to the partial thermal decomposition of poly-acrylonitrile (PAN) at elevated temperature (Fig. S2, SI). The synthesis of CoP/CNFs is then achieved using NaH_2PO_2 as the phosphorus source under a pyrolysis treatment in Ar (Fig. S3, SI). Finally, Ir nanoparticles are *in situ* grown on the surface of CoP/CNFs *via* a wet-chemical approach. FE-SEM (Fig. 1b) and TEM (Fig. 1c) analyses confirm the presence of irregularly distributed nanoparticles on the fibrous CNFs in the 600Ir–CoP/CNFs sample with an average fiber diameter of approximately 116.3 nm (Fig. 1d). For comparison, 200Ir–CoP/CNFs and 1000Ir–CoP/CNFs possess analogous fibrous architectures (Fig. S4 and S5, SI). TEM analysis indicates that the $IrCl_3$ dosage variation does not significantly alter Ir nanoparticle size; however, moderate aggregation tendencies emerge with an increasing precursor concentration, as evidenced in the 1000Ir–CoP/CNFs sample (Fig. 1c, S4b and S5b, SI). In addition, high-angle annular dark-field scanning TEM (HAADF-STEM) and elemental mappings (Fig. 1e) of 600Ir–CoP/CNFs also demonstrate that Ir nanoparticles are mostly adjacent to the CoP nanoparticles, with discernible interfaces between the two

phases. High-resolution TEM (HRTEM) analysis further reveals the distinct interaction between CoP nanoparticles with a lattice spacing of 0.19 nm assigned to its (211) crystal plane and Ir nanoparticles with a lattice spacing of 0.22 nm corresponding to its (111) crystal plane (Fig. 1f–h).[34–36] These characterization results illustrate the formation of an Ir–CoP heterostructure supported on the CNFs. Energy-dispersive X-ray spectroscopy (EDX) analysis corroborates the co-presence of Co, P, and Ir elements, validating successful synthesis of 600Ir–CoP/CNFs (Fig. 1i).

X-ray diffraction (XRD) analysis confirms the structural integrity of the catalyst system. As depicted in Fig. 2a, the diffraction peaks of Co/CNFs align precisely with the standard face-centered cubic Co phase (PDF#89-7093), verifying the successful fabrication of Co-loaded CNFs.[37,38] Subsequent phosphorization with NaH_2PO_2 as the P source results in the disappearance of Co peaks and the emergence of CoP signals, whose diffraction peaks correspond satisfactorily with the CoP phase (PDF#89-2598), signifying the conversion of metallic Co to CoP.[39,40] Furthermore, the XRD pattern of the obtained Ir–CoP/CNFs shows that the distinctive diffraction peaks of CoP remain pronounced after the modification of Ir nanoparticles on their surface. Notably, while low Ir loading attenuates
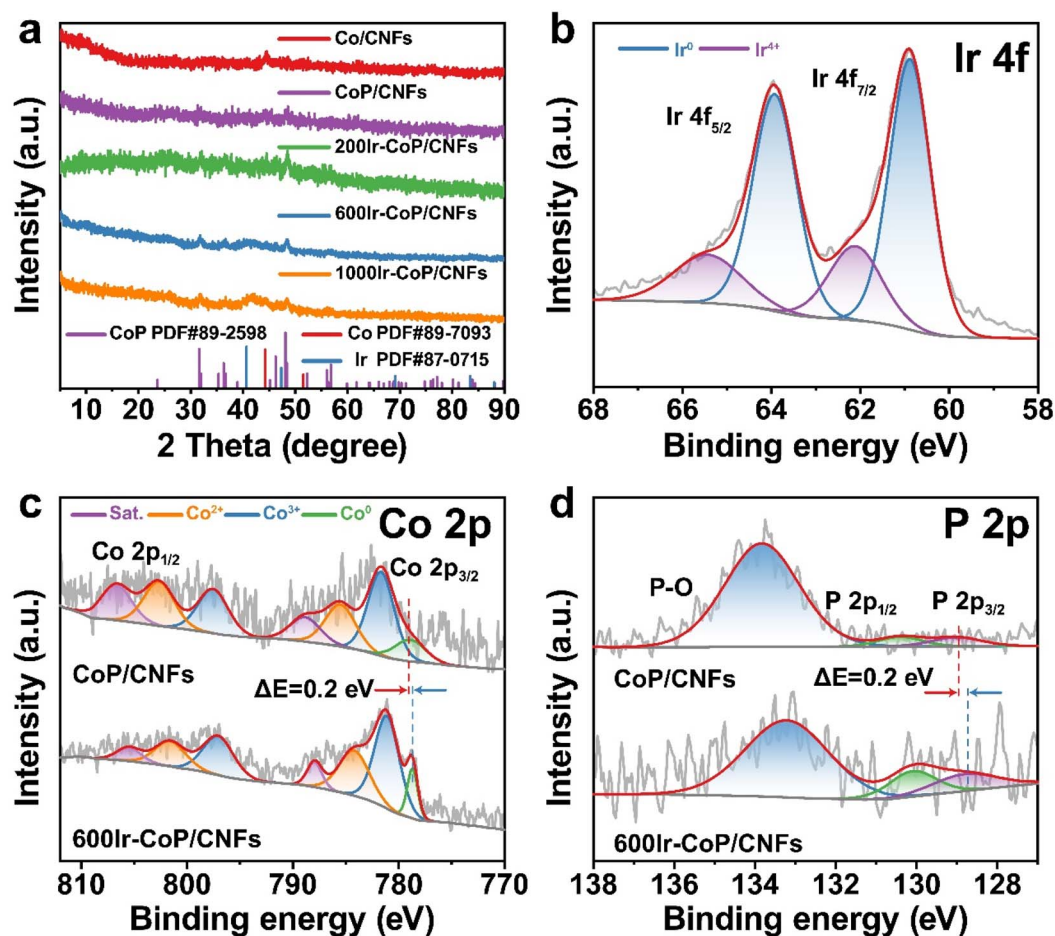

Fig. 2 (a) XRD patterns of Co/CNFs, CoP/CNFs, 200Ir–CoP/CNFs, 600Ir–CoP/CNFs and 1000Ir–CoP/CNFs. (b) Typical high-resolution Ir 4f XPS spectrum of 600Ir–CoP/CNFs. (c) Typical high-resolution Co 2p XPS spectra and (d) typical high-resolution P 2p XPS spectra of CoP/CNFs and 600Ir–CoP/CNFs.

characteristic peak intensities, the distinctive Ir (111) diffraction peak becomes discernible with an increased Ir content in 600Ir–CoP/CNFs and 1000Ir–CoP/CNFs samples.[41,42]

The chemical states of the catalyst are systematically analyzed using X-ray photoelectron spectroscopy (XPS) measurement. The full XPS spectrum of 600Ir–CoP/CNFs verifies the presence of Co, P, and Ir elements, signifying the effective Ir nanoparticles deposition onto the surface of CoP/CNFs (Fig. S6, SI). Detailed examination of the Ir 4f region in the XPS spectrum identifies the peaks at 60.9 eV and 63.9 eV, assigned to metallic Ir $4f_{7/2}$ and Ir $4f_{5/2}$, respectively, confirming the successful preparation of Ir nanoparticles (Fig. 2b).[20,43,44] Additionally, two other peaks are attributed to Ir^{4+}, which could be ascribed to the coordination interaction between Ir atoms and adjacent atoms, along with slight and inevitable surface oxidation. In the Co 2p XPS spectrum of CoP/CNFs, the peak at 778.7 eV is associated with Co^0, while the remaining six prominent peaks correspond to Co^{3+}, Co^{2+}, and their respective satellite peaks, indicative of a classic CoP structure (Fig. 2c).[45–47] Notably, compared to CoP/CNFs, the binding energy of the Co–P

bond in 600Ir–CoP/CNFs exhibits a pronounced shift towards lower binding energy. This observation suggests electron transfer from Ir to the CoP substrate, corroborating the results of theoretical computations in the later section. Furthermore, in the P 2p XPS spectrum, the peak at 133.2 eV is assigned to the P–O bond, while the peaks at 130.1 eV and 128.8 eV correspond to P $2p_{1/2}$ and P $2p_{3/2}$, respectively, which are associated with the Co–P bond (Fig. 2d).[47,48] Similar to the case of Co, the binding energy of P also shifts to lower values, further confirming the electronic modulation of the support by Ir nanoparticles. In essence, the observed shifts in the binding energies of Co 2p and P 2p in 600Ir–CoP/CNFs provide robust experimental evidence for the electronic modulation of the CoP support by Ir nanoparticles, benefiting the promoted electrocatalytic performance.

2.2 HER performance in an acidic medium

The electrocatalytic HER efficiencies of the catalysts are initially evaluated in 0.5 M H_2SO_4. The linear scan voltammetry (LSV) curves in Fig. 3a illustrate that the 600Ir–CoP/CNFs catalyst
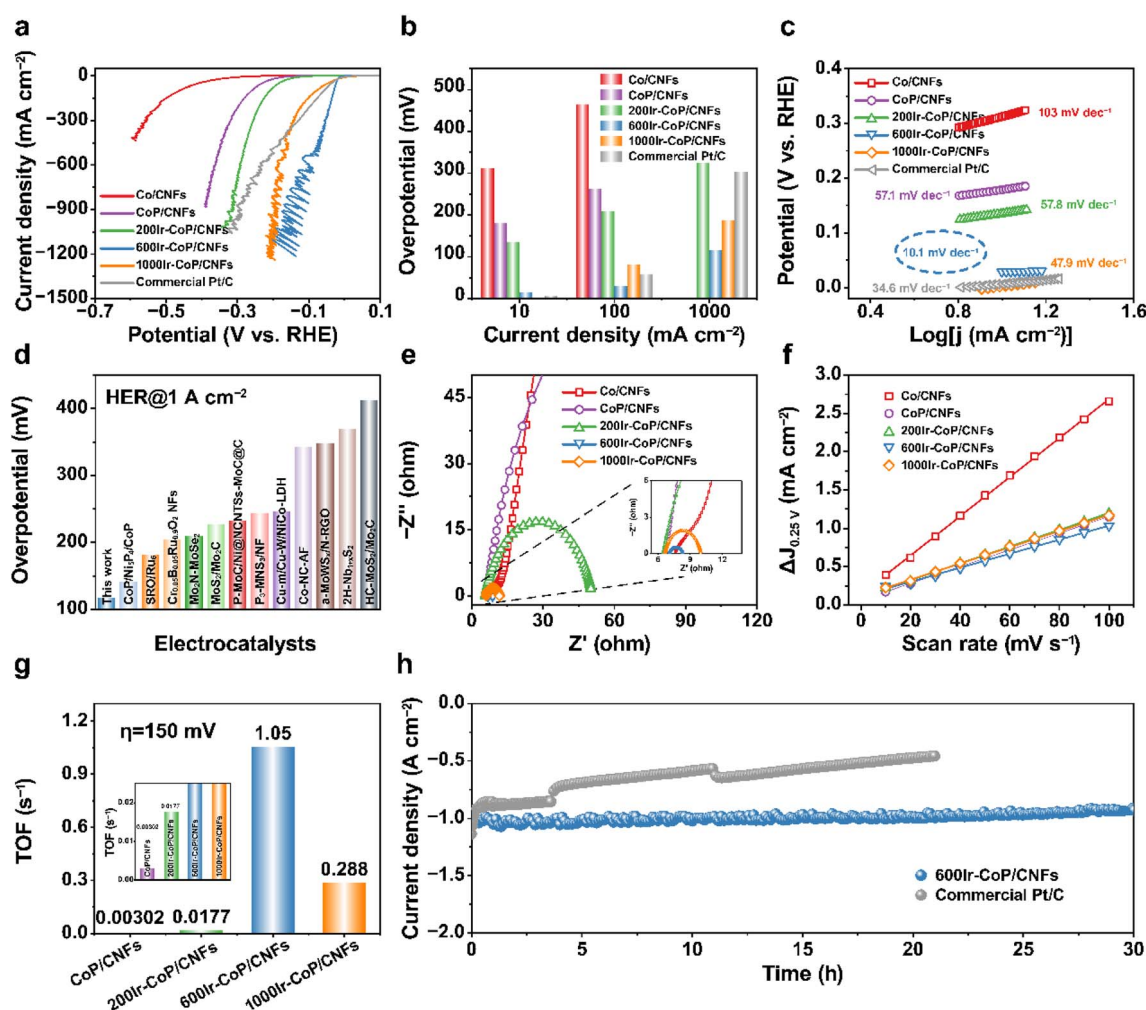

Fig. 3 HER tests in 0.5 M H_2SO_4. (a) LSV curves. (b) Overpotential comparison. (c) Tafel analysis. (d) Comparison of overpotentials at a current density of 1 A cm^{-2} for various HER electrocatalysts with iR-correction. (e) Nyquist plots. (f) C_{dl} value analysis. (g) TOF values. (h) I–t curves of 600Ir–CoP/CNFs and commercial Pt/C at $\approx$1 A cm^{-2}.

attains a current density of 100 mA cm^{-2} with an overpotential (η_{100}) of merely 29.5 mV, substantially outperforming the reference catalysts including Co/CNFs (465.5 mV), CoP/CNFs (261.9 mV), 200Ir–CoP/CNFs (209.5 mV), 1000Ir–CoP/CNFs (80.9 mV), and the commercial Pt/C catalyst (58.6 mV). Remarkably, at elevated current densities, 600Ir–CoP/CNFs exhibit exceptional performance, reaching 1.0 A cm^{-2} with an overpotential of only 117 mV, which is substantially lower than that of Pt/C (304 mV@1.0 A cm^{-2}) (Fig. 3b). These findings underscore the exceptional HER activity of 600Ir–CoP CNFs across a range of current densities. Notably, the LSV curves for both 600Ir–CoP/CNFs and 1000Ir–CoP/CNFs exhibit significant fluctuations as the current density increases (Fig. 3a). This characteristic "sawtooth" pattern arises from the formation and detachment of numerous H$_2$ bubbles during the vigorous HER process.[49–51] Furthermore, the Ir/CNFs catalyst is also prepared for comparison, exhibiting a lower HER activity than the target 600Ir–CoP/CNFs. This finding reveals that the improved HER performance of 600Ir–CoP/CNFs is not only due to the introduction of Ir nanoparticles but also the electronic synergy between CoP and Ir (Fig. S7). Fig. 3c reveals a Tafel slope of 10.1 mV dec^{-1} for 600Ir–CoP/CNFs, which is considerably lower than that of Co/CNFs (103 mV dec^{-1}), CoP/CNFs (57.1 mV dec^{-1}), 200Ir–CoP/CNFs (57.8 mV dec^{-1}), 1000Ir–CoP/CNFs (47.9 mV dec^{-1}), and even Pt/C (34.6 mV dec^{-1}), indicating markedly enhanced reaction kinetics for the HER. The observed ultralow Tafel slope for 600Ir–CoP/CNFs might be related to the elevated catalyst mass loading and the unavoidable contribution from the concurrent hydrogen oxidation process, being consistent with some other highly active HER electrocatalysts.[52,53] Subsequently, as depicted in Fig. 3d and Table S1, SI, we have benchmarked the overpotential of our optimized 600Ir–CoP/CNFs catalyst at 1.0 A cm^{-2} against values reported in the existing literature. The comparative analysis demonstrates that the 600Ir–CoP/CNFs catalyst exhibits not only superior catalytic activity but also faster reaction kinetics. The improvement in the electrocatalytic performance of the 600Ir–CoP/CNFs is further elucidated through electrochemical impedance spectroscopy (EIS) analysis (Fig. S8, SI). Fig. 3e shows that the 600Ir–CoP/CNFs catalyst exhibits the smallest semicircle radius among the control catalysts, signifying the lowest electrochemical impedance, which contributes to its superior HER activity. The low resistance of the catalyst is not only due to the EMSI between Ir and CoP, but also efficient electron transfer facilitated by the CNFs as the support for CoP and Ir species.

Electrochemically active surface area (ECSA) is a key metric for evaluating the electrocatalytic efficiency of a catalyst.[54] Herein, we have further quantified the electrochemical double-layer capacitance (C_{dl}) of the catalysts to ascertain their total ECSA for normalizing HER activity. By analyzing the cyclic voltammetry (CV) data at varied scan rates within the non-faradaic region (Fig. S9, SI), we have obtained C_{dl} values that correlate positively with the ECSA. As depicted in Fig. 3f and Table S2, SI, the Co/CNFs catalyst exhibits the highest C_{dl} and ECSA, indicative of the maximal exposure of active sites. Crucially, the ECSA-normalized current densities reveal that the 600 Ir–CoP/CNFs catalyst possesses a superior intrinsic HER activity

compared to the other catalysts (Fig. S10, SI). To assess the utilization of active sites and the intrinsic catalytic performance, the noble metal contents in the catalysts have been quantified via inductively coupled plasma optical emission spectroscopy (ICP-OES). It reveals that the Ir contents in 200Ir–CoP/CNFs, 600Ir–CoP/CNFs, and 1000Ir–CoP/CNFs are 3.63%, 7.89%, and 12.0%, respectively. Based on the ICP results, the turnover frequency (TOF) for the HER is computed (Table S3, SI). As illustrated in Fig. 3g, the 600Ir–CoP/CNFs catalyst achieves a TOF value of 1.05 s^{-1} at an overpotential of 150 mV, significantly exceeding that of the reference catalysts. These findings provide further evidence of the exceptional intrinsic catalytic activity of 600Ir–CoP/CNFs. The mass activity, based on the noble metal content, reaches 12 241 A g$_{NM}^{-1}$ at an overpotential of 150 mV for 600Ir–CoP/CNFs, which is 7.8-fold that of the commercial Pt/C catalyst and also substantially surpasses those of the other control catalysts (Fig. S11, SI). Although the Ir loading in 1000Ir–CoP/CNFs is higher than that in 600Ir–CoP/CNFs, excessive Ir content may lead to particle aggregation (Fig. S5b), resulting in consequently deteriorating the catalytic activity.[55–57] In addition to its high mass activity, the 600Ir–CoP/CNFs catalyst demonstrates excellent stability under conditions relevant to industrial applications. At 1.0 A cm^{-2}, it maintains 91.2% of its initial activity for 30 hours without significant decay (Fig. 3h). Post-stability analyses, including SEM images (Fig. S12a, SI) and XRD patterns (Fig. S13a, SI), confirm the preservation of the morphology, composition, and crystal structure of 600Ir–CoP/CNFs, emphasizing its robust structural and chemical stability as a highly efficient and stable HER catalyst with considerable potential for real-world applications. Post-reaction XPS analysis of 600Ir–CoP/CNFs (Fig. S14, SI) reveals a substantial decrease in the Ir^0/Ir^{4+} peak area ratio, indicating partial corrosion of Ir nanoparticles. Concurrently, a significant attenuation of the peak intensities of Co and P compared to the pristine catalyst suggests the dissolution of the CoP component. ICP-OES analysis of the post-reaction electrolyte validates this mechanism, demonstrating the dissolved Co accounting for 13.7% relative to the 600Ir–CoP/CNFs catalyst (Table S4, SI). This quantitative leaching evidence conclusively explains the attenuated Co and P signals observed in the XPS spectra.

2.3 HER performances in an alkaline electrolyte

The HER performance of the catalyst is further evaluated in an alkaline electrolyte (1 M KOH). At 10 mA cm^{-2}, the 600Ir–CoP/CNFs catalyst achieves an ultralow overpotential of 13.9 mV, which is better than that of the other control catalysts including Co/CNFs (240.9 mV), CoP/CNFs (232.6 mV), 200Ir–CoP/CNFs (164.3 mV), 1000Ir–CoP/CNFs (71.6 mV) and Ir/CNFs (71.8 mV) (Fig. 4a and S7b, SI). Crucially, at industrially relevant 1.0 A cm^{-2}, the 600Ir–CoP/CNFs catalyst exhibits a substantially lower overpotential of approximately 235 mV, significantly surpassing that of commercial Pt/C (356 mV at 1.0 A cm^{-2}) (Fig. 4b). This demonstrates practical viability under high-current-density conditions. Kinetic analysis reveals a Tafel slope of 14.3 mV dec^{-1} for 600Ir–CoP/CNFs, notably lower than that of
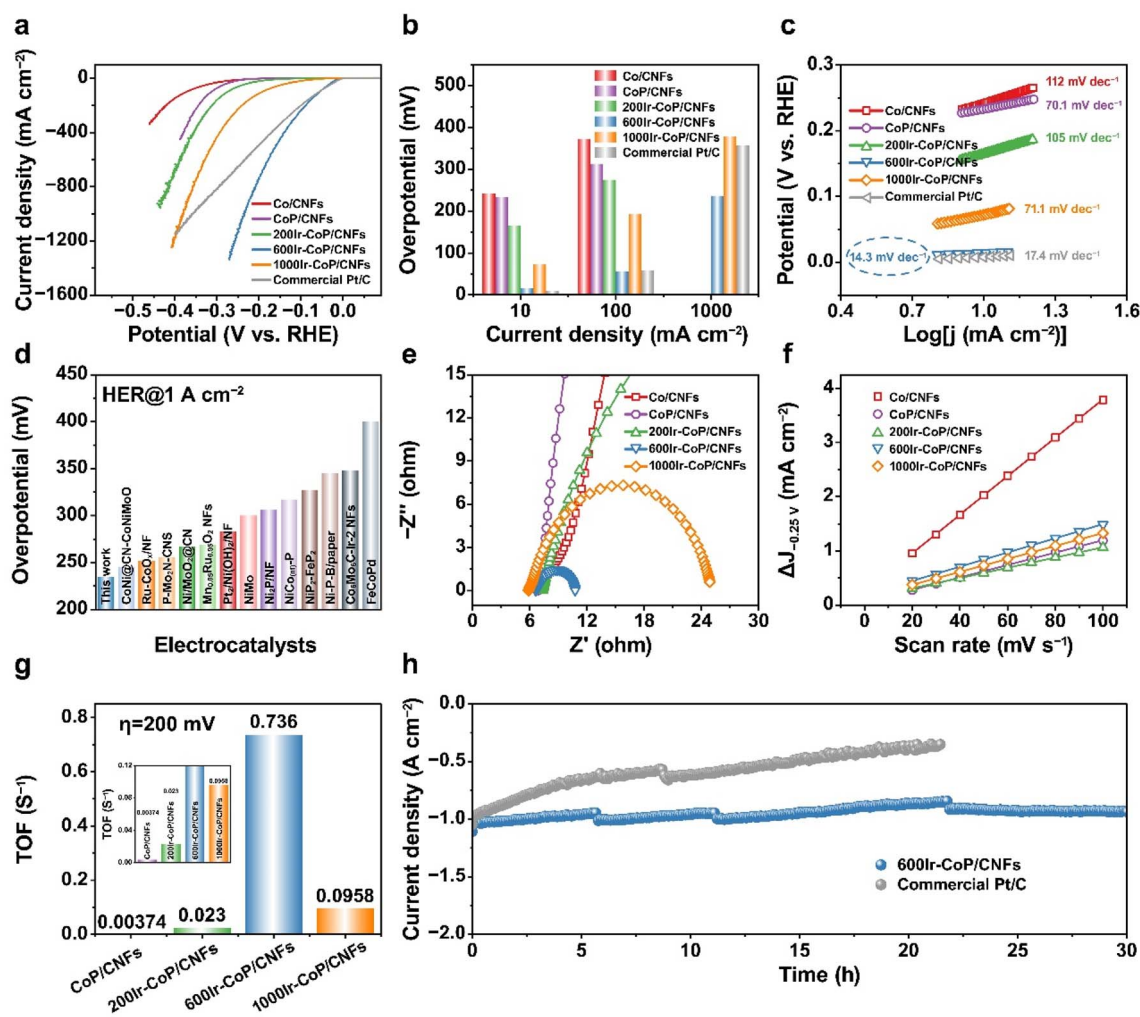
Fig. 4 HER tests in 1.0 M KOH. (a) LSV curves. (b) Overpotential comparison. (c) Tafel analysis. (d) Comparison of overpotentials at a current density of 1.0 A cm^{-2} for various HER electrocatalysts with *iR*-correction. (e) Nyquist plots. (f) C_{dl} values. (g) TOF values. (h) *I*–*t* curves of 600Ir–CoP/CNFs and commercial Pt/C at ≈1 A cm^{-2}.

Pt/C (17.4 mV dec^{-1}), underscoring its faster reaction kinetics (Fig. 4c). Benchmarking against literature data at 1.0 A cm^{-2} (Fig. 4d and Table S5, SI) reveals that 600Ir–CoP/CNFs not only exhibits comparable or superior catalytic activity but also faster reaction kinetics at high current densities. The superior electrocatalytic performance is further substantiated by electrochemical impedance spectroscopy (EIS) analysis. As depicted in Fig. 4e, the 600Ir–CoP/CNFs catalyst displays the lowest resistance among all tested materials, implying optimized electron transport properties essential for efficient electrocatalysis.

Furthermore, the ECSA values of the catalysts in an alkaline solution have also been estimated from the C_{dl} values (Fig. S15, SI). As shown in Fig. 4f and Table S6, SI, Co–C/CNFs demonstrates the highest ECSA, suggesting maximal active site exposure. Crucially, ECSA-normalized HER activity reveals that 600Ir–CoP/CNFs consistently outperforms comparators (Fig. S16, SI), further demonstrating its higher intrinsic alkaline HER activity. Similarly, the TOF is also computed to assess this advantage. As depicted in Fig. 4g, the 600Ir–CoP/CNFs catalyst

yields a TOF value of 0.736 s^{-1} at an overpotential of 200 mV, significantly exceeding that of reference catalysts. Based on the noble metal content, the mass activity of the 600Ir–CoP/CNFs catalyst reaches 8560 A g$_{NM}^{-1}$ at an overpotential of 200 mV (Fig. S17, SI), which is 3.8-fold that of the Pt/C catalyst and also markedly higher than that of the other control catalysts, emphasizing its standout performance and industrial applicability. Stability testing at industrial-level current density (1.0 A cm^{-2}) illustrates the maintenance of over 92.7% of its initial current density for 30 hours with negligible decay (Fig. 4h). Post-stability characterization studies confirm the preserved morphology and chemical structure of the 600Ir–CoP/CNFs following extended alkaline HER operation (Fig. S12b, S13b and S18, SI).

2.4 DFT calculations

To elucidate the high-efficiency HER mechanism of the Ir–CoP/CNFs across a broad pH range, density functional theory (DFT) calculations are conducted. This approach is aimed at investigating the electronic structure modulation and the complex

multi-step reaction kinetics inherent to this catalytic system. The presence of a distinct interface between Ir nanoparticles and CoP, as revealed by the EDX mapping and HRTEM analysis, leads to the construction of a theoretical model with Ir clusters anchored on a CoP slab (Fig. 5a, S19 and S20, SI). The subsequent geometric optimization reveals that there is a stable interface formation between Ir clusters and CoP. Differential charge density analysis demonstrates substantial charge redistribution at the interface (Fig. 5b), where electrons migrate from Ir to CoP, accumulating at their interface. Bader charge analysis confirms that approximately 0.16 electrons transfer from Ir to CoP, providing the evidence of the EMSI effect. To quantify this phenomenon, we perform work function analysis (Fig. 5c). The findings indicate a notable disparity in work functions between Ir nanoparticles (3.69 eV) and CoP (4.89 eV), driving electron transfer from metallic Ir to semiconducting CoP, which generates a built-in electric field oriented from CoP to Ir.[37,58] This observation further validates the EMSI at the Ir–CoP heterointerface. For the key elementary steps of the HER, the free energy of hydrogen intermediate (H*) adsorption (ΔG_{H*}) on various active sites is computed (Fig. 5d). The calculations reveal that H* adsorption on the Ir surface yields an optimal

ΔG_{H*} value of -0.23 eV, closely approaching the volcano peak ($\Delta G_{H*} = 0$ eV), whereas the Co site on the CoP displays a notably higher ΔG_{H*} of -0.33 eV (Fig. 5e). The ΔG_{H*} on the pristine CoP surface deviates substantially from the theoretically optimal value of 0 eV, signifying suboptimal electrocatalytic activity for the HER (Fig. S21, SI). This pronounced discrepancy can be ascribed to the synergistic effects between the metallic properties of Ir and interfacial charge transfer. The electron transfer from Ir to CoP results in an electron-deficient Ir surface, effectively moderating the strength of H* adsorption. Furthermore, we have employed the Climbing Image Nudged Elastic Band (CI-NEB) method to examine the comprehensive HER pathway under alkaline conditions (Fig. 5f).[59,60] Additionally, the water dissociation step ($H_2O^* \rightarrow OH^* + H^*$) necessitates overcoming an energy barrier of 1.16 eV on the pristine CoP surface, whereas at the Ir–CoP interface, this barrier is significantly reduced to 0.42 eV (Fig. 5g). These insights underscore that the directional reconstruction of interfacial electronic structures, in tandem with the precise optimization of multi-step reaction kinetics, collectively endows the Ir–CoP heterostructure with exceptional intrinsic HER efficiency across an extensive pH range.
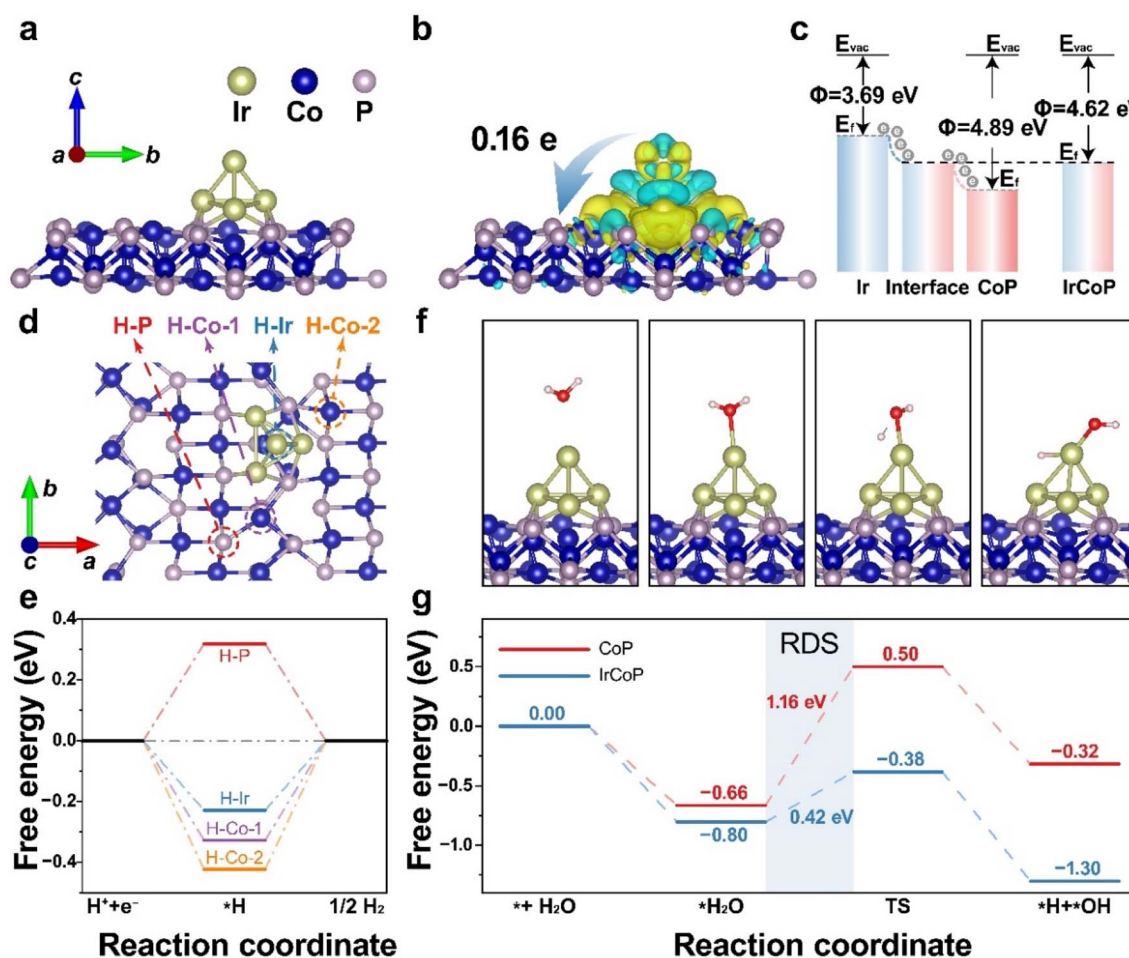

Fig. 5 DFT calculations of Ir–CoP and CoP for the HER. (a) The model of Ir–CoP. (b) Charge density of Ir–CoP, indicating electron gain (yellow) and loss (blue). (c) The work function of Ir, CoP, and Ir–CoP. (d) Sites of *H adsorption on the Ir–CoP model. (e) ΔG_{H*} on varied adsorption sites. (f) Intermediate adsorption configurations of water dissociation on Ir–CoP. (g) The kinetic barrier of water dissociation on Ir–CoP and CoP.

3. Conclusion

This study successfully engineers an efficient Ir–CoP/CNFs electrocatalyst for acidic/alkaline-universal HER. In this novel structure, the EMSI between Ir and CoP not only fine-tunes the electronic structure of the catalyst surface but also substantially diminishes the energy barriers for pivotal HER steps, including water dissociation and H* adsorption, culminating in highly efficient HER performance. Accordingly, the resultant optimized electrocatalyst presents a much better HER activity and durability than the state-of-the-art Pt/C catalyst at an ampere-grade current density. These findings offer critical theoretical guidance for the future design of HER catalysts and establish a robust theoretical framework for the progression of sustainable H_2 energy technology. This innovation of Ir–CoP/CNFs marks a significant milestone in the pursuit of more effective and robust catalysts for H_2 production, clearing a path for expanded applications in renewable energy systems.

Author contributions

X. Lu, W. Song and C. Wang supervised the project. L. Zhang performed the experiments, conducted theoretical calculations, and wrote the manuscript. L. Zhang, W. Li, S. Ren and Y. Zhang analyzed the data. All authors reviewed and approved the final manuscript.

Conflicts of interest

The authors declare no conflict of interest.

Data availability

The data supporting this article have been included as part of the SI. The SI includes detailed experimental procedures, additional characterization and electrochemical performance data.

Supplementary information is available. See DOI: **https://doi.org/10.1039/d5sc03067f**.

Acknowledgements

References

1 M. Pehl, A. Arvesen, F. Humpenöder, A. Popp, E. G. Hertwich and G. Luderer, *Nat. Energy*, 2017, **2**, 939–945.

2 K. Peng, K. Feng, B. Chen, Y. Shan, N. Zhang, P. Wang, K. Fang, Y. Bai, X. Zou, W. Wei, X. Geng, Y. Zhang and J. Li, *Nat. Commun.*, 2023, **14**, 3144.

3 L. Zhang, W. Li, S. Ren, W. Song, C. Wang and X. Lu, *Adv. Energy Mater.*, 2025, **15**, 2403136.

4 W. Li, C. Wang and X. Lu, *Nano Lett.*, 2024, **24**, 11779–11792.

5 W. Li, L. Zhang, L. Ma, J. Wang, R. Qi, Y. Pang, M. Xu, C. Zhao, C. Wang, M. Gao and X. Lu, *Nano Lett.*, 2025, **25**, 443–452.

6 J. A. Turner, *Science*, 2004, **305**, 972–974.

7 J. Zhu, L. S. Hu, P. X. Zhao, L. Y. S. Lee and K. Y. Wong, *Chem. Rev.*, 2020, **120**, 851–918.

8 J. Wang, F. Xu, H. Y. Jin, Y. Q. Chen and Y. Wang, *Adv. Mater.*, 2017, **29**, 1605838.

9 J. Mahmood, F. Li, S. M. Jung, M. S. Okyay, I. Ahmad, S. J. Kim, N. Park, H. Y. Jeong and J. B. Baek, *Nat. Nanotechnol.*, 2017, **12**, 441–446.

10 W. Song, M. Li, C. Wang and X. Lu, *Carbon Energy*, 2021, **3**, 101–128.

11 W. Li, C. Wang and X. Lu, *J. Mater. Chem. A*, 2021, **9**, 3786–3827.

12 F. Guo, T. J. Macdonald, A. J. Sobrido, L. X. Liu, J. R. Feng and G. J. He, *Adv. Sci.*, 2023, **10**, 2301098.

13 Z. Zeb, Y. C. Huang, L. L. Chen, W. B. Zhou, M. H. Liao, Y. Y. Jiang, H. T. Li, L. M. Wang, L. Wang, H. Wang, T. Wei, D. J. Zang, Z. J. Fan and Y. G. Wei, *Coord. Chem. Rev.*, 2023, **482**, 215058.

14 H. Tüysüz, *Acc. Chem. Res.*, 2024, **57**, 558–567.

15 T. Hrbek, P. Kús, J. Drnec, M. Mirolo, H. Nedumkulam, I. Martens, J. Nováková, T. Skála and I. Matolínová, *Adv. Energy Mater.*, 2025, **15**, 2403738.

16 X. Chen, W. Gou, J. Xu, R. Qi, S. Ren, C. Wang, W. Chen, G. Yu and X. Lu, *Chem. Eng. J.*, 2023, **471**, 144481.

17 C. Liu, G. Pan, N. Liang, S. Hong, J. Ma and Y. Liu, *Adv. Sci.*, 2022, **9**, 2105392.

18 H. Ding, C. Su, J. Wu, H. Lv, Y. Tan, X. Tai, W. Wang, T. Zhou, Y. Lin, W. Chu, X. Wu, Y. Xie and C. Wu, *J. Am. Chem. Soc.*, 2024, **146**, 7858–7867.

19 M. Huang, H. Yang, X. Xia and C. Peng, *Appl. Catal., B*, 2024, **358**, 124422.

20 W. Li, W. Gou, L. Zhang, M. Zhong, S. Ren, G. Yu, C. Wang, W. Chen and X. Lu, *Chem. Sci.*, 2024, **15**, 11890–11901.

21 J. Zhang, Q. Y. Zhang and X. L. Feng, *Adv. Mater.*, 2019, **31**, 1808167.

22 B. Zhang, J. Wang, G. Liu, C. M. Weiss, D. Liu, Y. Chen, L. Xia, P. Zhou, M. Gao, Y. Liu, J. Chen, Y. Yan, M. Shao, H. Pan and W. Sun, *Nat. Catal.*, 2024, **7**, 441–451.

23 P. Kuang, Y. Wang, B. Zhu, F. Xia, C. W. Tung, J. Wu, H. M. Chen and J. Yu, *Adv. Mater.*, 2021, **33**, 2008599.

24 M. Xie, F. Dai, H. Guo, P. Du, X. Xu, J. Liu, Z. Zhang and X. Lu, *Adv. Energy Mater.*, 2023, **13**, 2203032.

25 J. Deng, P. J. Ren, D. H. Deng and X. H. Bao, *Angew. Chem., Int. Ed.*, 2015, **54**, 2100–2104.

26 Z. Yu, Y. Li, A. Torres-Pinto, A. P. LaGrow, V. M. Diaconescu, L. Simonelli, M. J. Sampaio, O. Bondarchuk, I. Amorim, A. Araujo, A. M. T. Silva, C. G. Silva, J. L. Faria and L. Liu, *Appl. Catal., B*, 2022, **310**, 121318.

27 H. Yang, P. Guo, R. Wang, Z. Chen, H. Xu, H. Pan, D. Sun, F. Fang and R. Wu, *Adv. Mater.*, 2022, **34**, 2107548.

28 J. Q. Tian, Q. Liu, A. M. Asiri and X. P. Sun, *J. Am. Chem. Soc.*, 2014, **136**, 7587–7590.

29 S. Shen, Z. Wang, Z. Lin, K. Song, Q. Zhang, F. Meng, L. Gu and W. Zhong, *Adv. Mater.*, 2022, **34**, 2110631.

30 J. Li, Y. Tan, M. Zhang, W. Gou, S. Zhang, Y. Ma, J. Hu and Y. Qu, *ACS Energy Lett.*, 2022, **7**, 1330–1337.

31 H. Song, M. Wu, Z. Tang, J. S. Tse, B. Yang and S. Lu, *Angew. Chem., Int. Ed.*, 2021, **60**, 7234–7244.

32 Z. Wang, K. Chi, S. Yang, J. Xiao, F. Xiao, X. Zhao and S. Wang, *Small*, 2023, **19**, 2301403.

33 Y. Zhu, J. Li, G. Zhou, L. Qian, Y. Fang, M. Xu, H. Pang, M. Zhang, J. Xu, J. Yang, L. Xu and Y. Tang, *Adv. Sustainable Syst.*, 2024, 2400041.

34 Y. Dong, Z. Deng, Z. Xu, G. Liu and X. Wang, *Small Methods*, 2023, **7**, 2300071.

35 K. Hayashi, T. Tomimori, Y. Chida, N. Todoroki and T. Wadayama, *J. Phys. Chem. C*, 2021, **125**, 21481–21487.

36 K. Zhang, J. Jia, E. Yang, S. Qi, H. Tian, J. Chen, J. Li, Y. Lou and Y. Guo, *Nano Energy*, 2023, **114**, 108601.

37 Y. Feng, S. Long, G. Yan, W. Jia, Y. Sun, X. Tang, Z. Zhang, X. Zeng and L. Lin, *J. Catal.*, 2021, **397**, 148–155.

38 M. Qiao, Y. Wang, T. Wågberg, X. Mamat, X. Hu, G. Zou and G. Hu, *J. Energy Chem.*, 2020, **47**, 146–154.

39 T. Liu, X. Yu, S. Yu, H. Yang, Q. Sun, C. Wang, S. Li and J. Y. Zheng, *J. Alloys Compd.*, 2024, **973**, 172886.

40 Z. Li, L. Zhang, X. Ge, C. Li, S. Dong, C. Wang and L. Yin, *Nano Energy*, 2017, **32**, 494–502.

41 C. Li, W. Zhang, Y. Cao, J. Y. Ji, Z. C. Li, X. Han, H. Gu, P. Braunstein and J. P. Lang, *Adv. Sci.*, 2024, 2401780.

42 X. Wu, Z. Wang, K. Chen, Z. Li, B. Hu, L. Wang and M. Wu, *ACS Appl. Mater. Interfaces*, 2021, **13**, 22448–22456.

43 S. S. Karade, R. Sharma, S. Gyergyek, P. Morgen and S. M. Andersen, *ChemCatChem*, 2023, **15**, e202201470.

44 D. Zhao, Y. Zhu, Q. Wu, W. Zhou, J. Dan, H. Zhu, W. Lei, L. J. Ma and L. Li, *Chem. Eng. J.*, 2022, **430**, 132825.

45 P. Arunkumar, S. Gayathri and J. H. Han, *ACS Appl. Energy Mater.*, 2022, **5**, 2975–2992.

46 H.-Y. Wang, L. Wang, J.-T. Ren, W. Tian, M. Sun, Y. Feng and Z.-Y. Yuan, *ACS Nano*, 2023, **17**, 10965–10975.

47 F. Zhang, X. Wang, W. Han, Y. Qian, L. Qiu, Y. He, L. Lei and X. Zhang, *Adv. Funct. Mater.*, 2023, **33**, 2212381.

48 X. Yang, A.-Y. Lu, Y. Zhu, M. N. Hedhili, S. Min, K.-W. Huang, Y. Han and L.-J. Li, *Nano Energy*, 2015, **15**, 634–641.

49 R. Iwata, L. Zhang, K. L. Wilke, S. Gong, M. He, B. M. Gallant and E. N. Wang, *Joule*, 2021, **5**, 887–900.

50 R. Liu, Z. Gong, J. Liu, J. Dong, J. Liao, H. Liu, H. Huang, J. Liu, M. Yan, K. Huang, H. Gong, J. Zhu, C. Cui, G. Ye and H. Fei, *Adv. Mater.*, 2021, **33**, 2103533.

51 P. A. Kempler, R. H. Coridan and L. Luo, *Chem. Rev.*, 2024, **124**, 10964–11007.

52 C. Wan, Y. Ling, S. Wang, H. Pu, Y. Huang and X. Duan, *ACS Cent. Sci.*, 2024, **10**, 658–665.

53 X. Yu, M. Xia, R. Qi, Y. Wang, M. Gao, M. Zhong and X. Lu, *Chem. Sci.*, 2025, **16**, 10042–10050.

54 Z. Yu, G. Xia, V. M. Diaconescu, L. Simonelli, A. P. LaGrow, Z. Tai, X. Xiang, D. Xiong and L. Liu, *Chem. Sci.*, 2024, **15**, 9216–9223.

55 W. Wang, Y. Wu, Y. Lin, J. Yao, X. Wu, C. Wu, X. Zuo, Q. Yang, B. Ge, L. Yang, G. Li, S. Chou, W. Li and Y. Jiang, *Adv. Funct. Mater.*, 2022, **32**, 2108464.

56 G. Zhao, P. Li, N. Cheng, S. X. Dou and W. Sun, *Adv. Mater.*, 2020, **32**, 2000872.

57 Y. Zhu, M. Klingenhof, C. Gao, T. Koketsu, G. Weiser, Y. Pi, S. Liu, L. Sui, J. Hou, J. Li, H. Jiang, L. Xu, W.-H. Huang, C.-W. Pao, M. Yang, Z. Hu, P. Strasser and J. Ma, *Nat. Commun.*, 2024, **15**, 1447.

58 B. Fang, Z. Xing, W. Kong, Z. Li and W. Zhou, *Nano Energy*, 2022, **101**, 107616.

59 G. Henkelman and H. Jónsson, *J. Chem. Phys.*, 2000, **113**, 9978–9985.

60 G. Henkelman, B. P. Uberuaga and H. Jónsson, *J. Chem. Phys.*, 2000, **113**, 9901–9904.